Efficient Double-Quantum Excitation in Rotational Resonance NMR

T. Karlsson, M. Edén, H. Luthman, and M. H. Levitt[1]

Division of Physical Chemistry, Arrhenius Laboratory, Stockholm University, S-106 91 Stockholm, Sweden

We present a new technique for double-quantum excitation in magic-angle-spinning solid-state NMR. The method involves (i) preparation of nonequilibrium longitudinal magnetization; (ii) mechanical excitation of zero-quantum coherence by spinning the sample at rotational resonance, and (iii) phase-coherent conversion of the zero-quantum coherence into double-quantum coherence by frequency-selective spin inversion. The double-quantum coherence is converted into observable magnetization by reversing the excitation process, followed by a $\pi/2$ pulse. The method is technically simple, does not require strong RF fields, and is feasible at high spinning frequencies. In $[^{13}C_2,^{15}N]$-glycine, with an internuclear $^{13}C-^{13}C$ distance of 0.153 nm, we achieve a double-quantum filtering efficiency of $\approx 56\%$. In $[11,20-^{13}C_2]$-all-*E*-retinal, with an internuclear $^{13}C-^{13}C$ distance of 0.296 nm, we obtain $\approx 45\%$ double-quantum filtering efficiency. © 2000 Academic Press

Key Words: multiple-quantum coherence; double-quantum coherence; zero-quantum coherence; rotational resonance; magic-angle spinning.

I. INTRODUCTION

Multiple-quantum techniques are becoming increasingly important in the NMR of magic-angle-spinning (MAS) solids. Multiple-quantum coherences are exploited to improve spectral resolution (*1*), to suppress signals from isolated spins-1/2 (*2–11*), and to estimate local molecular structure through internuclear distances (*12–18*) and molecular torsion angles (*17–26*).

It is difficult to excite multiple-quantum coherence with high efficiency in powdered solids. In systems of coupled spins-1/2, the excitation of double- or zero-quantum coherence requires the participation of the isotropic *J*-coupling or the direct dipole–dipole coupling. The *J*-couplings are usually small, but have been used successfully in some cases (*27*). The direct dipole–dipole couplings are difficult to exploit because they are strongly orientation-dependent and are usually efficiently quenched by the magic-angle sample rotation.

Most multiple-quantum excitation methods use applied RF fields to recouple the homonuclear dipole–dipole interactions in the presence of magic-angle spinning (*4–11*). In favorable cases, it is possible to pass as much as 73% of the $^{13}C_2$ spin-pair signal through multiple-quantum coherence (*6–10*).

Radiofrequency recoupling methods are often limited by the difficulty of implementing heteronuclear decoupling during the multiple-pulse sequence. In the case of ^{13}C recoupling in organic solids, intense RF irradiation is applied at the ^1H Larmor frequency while the ^{13}C multiple-quantum excitation is under way. The required RF fields are usually directed proportional to the spinning frequency. For example, in the case of C7 (*7*), the RF field on the recoupled species *S* (e.g., ^{13}C) corresponds to a nutation frequency of seven times the spinning frequency, $\omega_{nut}^S = 7\omega_r$. Effective heteronuclear decoupling requires a nutation frequency for the second spin species *I* (e.g., ^1H) which is large enough to satisfy $\omega_{nut}^I \gtrsim 3\omega_{nut}^S$ (*9*). Technical limitations on probe performance limit the application of such sequences to spinning frequencies of around 6 kHz. Recent developments relax these requirements somewhat (*10, 11*), but the difficulties associated with heteronuclear decoupling are still expected to present a considerable obstacle in many contexts.

In this paper, we present an approach based on *rotational resonance* (*28–35*), a phenomenon in which spin recoupling is achieved without RF irradiation. This greatly simplifies the task of heteronuclear decoupling, allowing the use of efficient modulation schemes (*36–38*) and making it possible to achieve good multiple-quantum excitation efficiencies, even at high spinning frequencies, without using a complicated RF pulse sequence.

Rotational resonance is established if a small integer multiple of the spinning frequency ω_r matches the isotropic shift frequency difference of two spin sites, denoted *j* and *k*,

$$\omega_j^{iso} - \omega_k^{iso} = n\omega_r, \qquad [1]$$

where *n* denotes the order of the rotational resonance. Under these conditions, the homonuclear dipole–dipole coupling participates in a resonant exchange of energy between the macroscopic sample rotation and the nuclear spins. Rotational resonance leads to spectral broadening and splitting as well as an enhanced exchange of longitudinal magnetization between the spin sites (*29–31*).

Nielsen *et al.* (*32*) exploited rotational resonance for double-quantum excitation in MAS solids. Transverse ^{13}C magnetization was allowed to evolve at the $n = 1$ rotational resonance

and converted into double-quantum coherence by applying a $\pi/2$ pulse. Around 25% of the ^{13}C signal was passed through double-quantum coherence for a compound with directly bonded ^{13}C–^{13}C pairs.

One factor limiting the efficiency of this method is its unfavorable orientation dependence. In general, three Euler angles are required to describe the orientation of a molecule with respect to the sample holder (see below). In a powder, all three angles are stochastic variables. The rotational resonance double-quantum excitation method described by Nielsen *et al.* (*32*) depends (in ideal circumstances) on two of the three angles. This strong orientation dependence degrades the efficiency of the excitation.

In this article, we excite double-quantum coherence in a different way, namely by exploiting the mechanical excitation of zero-quantum coherence at rotational resonance.

At rotational resonance, a differential in longitudinal magnetization of the two sites is spontaneously converted into zero-quantum coherence by the sample rotation itself. This process is rapid and efficient, and the amplitude of the zero-quantum coherence depends on only one of the three orientational Euler angles, in ideal circumstances. The zero-quantum coherence may readily be transferred into double-quantum coherence by a selective π rotation of one of the spins in each coupled spin pair. In the work described below, this selective π-rotation is achieved by a simple RF pulse sequence consisting of three pulses separated by two delays. Reconversion of the double-quantum coherence into zero-quantum coherence is carried out by a further selective inversion sequence, and rotational resonance drives the zero-quantum coherences back to the initial state of longitudinal difference magnetization, which may be converted into observable signal by a strong $\pi/2$ pulse.

This method is very efficient because the relevant transfer steps *zero-quantum coherence* $\Rightarrow$ *double-quantum coherence* $\Rightarrow$ *zero-quantum coherence* all proceed rapidly and retain full control of the coherence phases. The reconstruction of longitudinal magnetization at the end of the pulse sequence has the form of a three-dimensional rotational resonance echo (*33, 34*), and occurs with high efficiency in a powder. In ideal circumstances a double-quantum filtering efficiency of $\sim$73% is achievable.

In principle, sequences such as C7 and variants (*8, 9*) achieve the same theoretical double-quantum coherence filtering efficiency. However, the rotational resonance method permits a much faster excitation and does not require strong RF fields on two irradiation channels.

For $^{13}C_2$-labeled glycine, with an internuclear ^{13}C–^{13}C distance of 0.153 nm (*39*), we were able to pass the ^{13}C signals through double-quantum coherences with an experimental efficiency of $\simeq$56%, at the $n = 1$ rotational resonance.

In [11,20–$^{13}C_2$]-all-*E*-retinal, which has a ^{13}C–^{13}C internuclear distance of 0.296 nm (*40*), we achieve $\simeq$45% double-
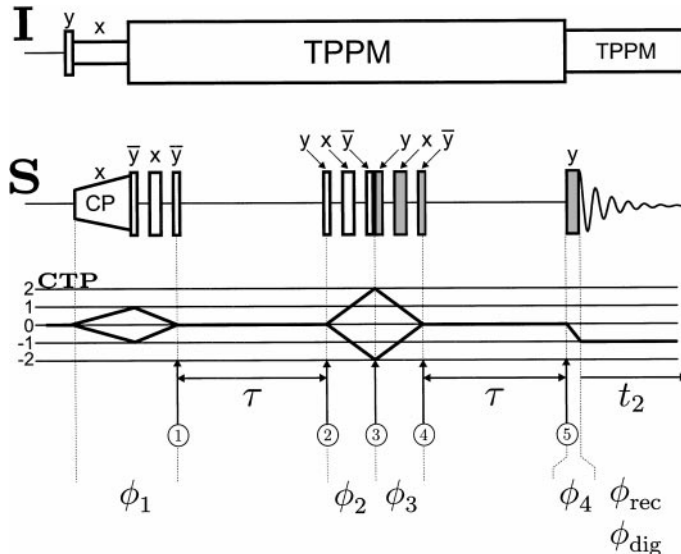

FIG. 1. Pulse sequence for excitation of double-quantum coherence at rotational resonance and associated coherence transfer pathway diagram.

quantum filtering efficiency at the $n = 1$ rotational resonance condition.

The method described here may be compared with the DREAM sequence of Verel *et al.* (*3*), which has achieved very high spin-pair selectivity ($\simeq$80%) in some circumstances. Although the DREAM sequence does pass spin-pair NMR signals through a double-quantum state, the passage occurs at different times for different molecular orientations, so the overall double-quantum filtering efficiency of DREAM, at any one time, is relatively low. As a result, it is not possible to exploit the high efficiency of DREAM for double-quantum determinations of molecular geometry. The rotational resonance method described here is a true double-quantum excitation method and may be used for any experiment that requires double-quantum coherence, providing that the isotropic chemical shifts are sufficiently well-separated.

Like all rotational resonance techniques, the method is very selective for spin pairs with isotropic shift differences satisfying the rotational resonance condition. In some cases, this is a serious limitation. In other situations, such as in multiple-spin systems, the high degree of selectivity may lead to a useful simplification of the spin dynamics.

II. PULSE SEQUENCE

Figure 1 shows the RF pulse sequence for rotational resonance excitation of double-quantum coherence through a mechanically excited zero-quantum state. The coherence transfer pathway diagram shows the history of coherence orders contributing to the final NMR signal. The pulse sequence is suitable for organic solids containing isolated pairs of ^{13}C spins (denoted S), as well as abundant ^1H spins (denoted I). The

reference frequency of the S-spin channel is denoted ω_{ref} and is given in terms of the S-spin carrier frequency by $\omega_{\text{ref}} = -\omega_{\text{carrier}}\text{sign}(\gamma)$ (41, 42), where γ is the magnetogyric ratio of the spins. The reference frequency is selected to be equal to the mean of the isotropic shift frequencies of the S-spin sites j and k, i.e., $\omega_{\text{ref}} = \frac{1}{2}(\omega_j^{\text{iso}} + \omega_k^{\text{iso}})$. The pulse sequence assumes that the $n = 1$ rotational resonance condition is satisfied, $\omega_\Delta^{\text{iso}} = \omega_r$ where $\omega_\Delta^{\text{iso}} = \omega_j^{\text{iso}} - \omega_k^{\text{iso}}$.

The circled numbers ①–⑤ denote specific time points within the pulse sequence. The symbols $\phi_1 \ldots \phi_5$, ϕ_{rec} denote the overall RF phases of pulse sequence blocks. The symbol ϕ_{rec} denotes the radiofrequency phase during signal detection, while the symbol ϕ_{dig} denotes the phase shift applied to the digitized complex signal (postdigitization phase shift). These phases are described in detail in Refs. (41) and (42). All symbols take into account the sign of the Larmor frequency and the mixing scheme of the RF signals (41, 42).

The pulse sequence starts by a ramped cross-polarization sequence which transfers magnetization from the abundant I-spins to the S-spins (43, 44). For the rest of the sequence, a two-pulse phase modulation scheme (TPPM) is applied on the I-spin channel (36).

The cross-polarization sequence creates transverse S-spin magnetization along the x-axis in the rotating frame. This is followed by a sequence of three strong RF pulses $(\pi/4)_{\bar{y}}-\Delta-(\pi/2)_x-\Delta-(\pi/4)_{\bar{y}}$, where the interval between the pulses is $\Delta = \tau_r/2$ and the sample rotation period is defined $\tau_r = |2\pi/\omega_r|$. This three-pulse sequence transforms the cross-polarized transverse magnetization into longitudinal magnetization, with opposite signs for the two spin sites, while partially compensating for chemical shift anisotropy. The operation of this sequence is discussed below.

In the following interval τ, the longitudinal difference magnetization at time point ① is converted into zero-quantum coherence by the mechanical rotation of the sample, under the influence of the homonuclear dipole–dipole couplings. The optimum excitation interval τ depends on the size of the through-space couplings. At the $n = 1$ rotational resonance, the optimal interval τ is given approximately by $\tau \simeq |2^{1/2}\pi/b_{jk}|$, where $b_{jk} = -(\mu_0/4\pi)\gamma_j\gamma_k\hbar/r_{jk}^3$ is the dipole–dipole coupling constant expressed in rads^{-1}, and r_{jk} is the internuclear distance.

A second three-pulse sequence $(\pi/4)_y-\Delta-(\pi/2)_x-\Delta-(\pi/4)_{\bar{y}}$ is applied between time points ② and ③. This sequence converts the zero-quantum coherence into double-quantum coherence with high efficiency and full preservation of phases (see below).

A third three-pulse sequence, applied between time point ③ and time point ④, converts the double-quantum coherence back into zero-quantum coherence, again with full transfer of the phase information. The zero-quantum coherence is driven mechanically into longitudinal magnetization during the following interval τ, forming a rotational resonance echo of longitudinal difference magnetization at time point ⑤.

The longitudinal difference magnetization is converted into

transverse difference magnetization by a strong nonselective $\pi/2$ pulse, and the NMR signal is collected in the subsequent time interval t_2. Fourier transformation of the NMR signal yields an NMR spectrum with opposite signs for the peaks associated with the two spin sites.

The signal passing through double-quantum coherence at time point ③ is collected by cycling the phases of the pulse sequence blocks according to standard procedures (45). The phases of the pulse sequence blocks $\phi_1, \phi_2 \ldots \phi_4$ and the RF receiver phase ϕ_{rec} are cycled according to

$$\phi_1 = \frac{2\pi m}{n_1}$$

$$\phi_p = \frac{2\pi}{n_p} \text{floor}\left(\frac{m}{n_1 n_2 \ldots n_{p-1}}\right), \quad (\text{for } 2 \leq p \leq 4),$$

$$\phi_{\text{rec}} = = \frac{2\pi m}{4} \qquad [2]$$

where the function floor(x) returns the largest integer not greater than x. Here m is the transient counter, $m = 0, 1 \ldots n_{tot} - 1$, where n_{tot} is the number of transients in a complete phasecycle, $n_{tot} = n_1 n_2 n_3 n_4$. In the present case, the cycling parameters were $n_1 = 1$; $n_2 = 1$; $n_3 = 4$; $n_4 = 2$; $n_{tot} = 8$. On each transient, the postdigitization phase ϕ_{dig} was adjusted to satisfy the equation

$$\phi_{\text{dig}} = -2\phi_2 + 2\phi_3 + \phi_4 - \phi_{\text{rec}}. \qquad [3]$$

This phase cycle selects signals passing through (± 2)-quantum coherence at time point ③ in Fig. 1.

The phases of the individual RF pulses are specified with respect to the phases of the blocks ϕ_1, ϕ_2, ϕ_3, and ϕ_4 according to the notation x, y, $\bar{x}$, $\bar{y}$ in Fig. 1. For example, the last three-pulse sequence which is notated $\{y, x, \bar{y}\}$ has the RF phases $\{\phi_3 + \pi/2, \phi_3, \phi_3 - \pi/2\}$. The final $\pi/2$ pulse has the phase $\phi_4 + \pi/2$.

III. THEORY

Frequency-Selective Spin Inversion

The double-quantum excitation scheme discussed here is based on the conversion of zero-quantum coherence into double-quantum coherence, and vice versa, through the selective inversion of spins in one of the coupled sites.

There have been many proposed methods for accomplishing a selective spin inversion. Early applications of rotational resonance employed a long weak RF pulse, or a long train of short pulses, at the Larmor frequency of one of the sites (46, 47). These methods lead to losses through relaxation and are susceptible to interference with the chemical shift anisotropy (CSA). In addition it is difficult to achieve good selec-
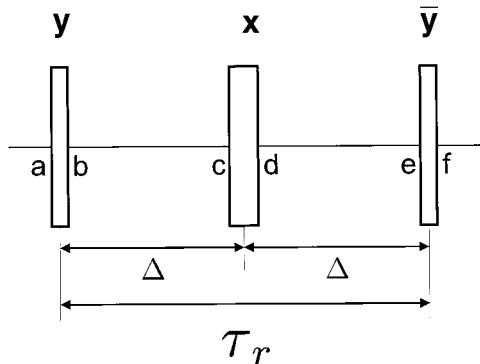
FIG. 2. Expanded view of the second and third three-pulse sequences.

tivity. It is also possible to use a free precession delay in conjunction with two strong $\pi/2$ pulses. However, this method is also sensitive to chemical shift anisotropy. Sequences of four or five π pulses were developed in order to compensate the spin evolution accurately for chemical shift anisotropy (48). These methods are rather elaborate and are susceptible to pulse imperfections. In the current paper, we employ a relatively simple three-pulse sequence which is partially compensated for the chemical shift anisotropy of one of the two sites. This sequence is well suited to most applications of rotational resonance since, in many cases, only one of the two coupled sites has a large chemical shift anisotropy.

The pulse sequence in Fig. 1 employs three such three-pulse sequences. The first three-pulse sequence is a little different from the others and will be examined later. We consider now the second and third three-pulse sequences, using an analysis method that was originally developed in the context of composite pulses (49, 50).

The second three-pulse sequence is presented on an expanded scale in Fig. 2. The phases denote the directions of the spin nutation axes, taking into account the sense of the Larmor precession, as described in Refs. (41, 42). The sequence lasts one full rotor period τ_r and consists of two $\pi/4$ pulses and one $\pi/2$ pulse. The sequence assumes that the $n = 1$ rotational resonance condition is satisfied, $\omega_\Delta^{\mathrm{iso}} = \omega_j^{\mathrm{iso}} - \omega_k^{\mathrm{iso}} = \omega_r$. In the discussion below, we assume that j denotes the most shielded site, and k denotes the least shielded site, i.e., $\omega_\Delta^{\mathrm{iso}} > 0$ in the case of spins with a positive magnetogyric ratio (41, 42).

The propagator of the three-pulse sequence may be written

$$U_{3P} = R_y\left(-\frac{\pi}{4}\right) U_{\mathrm{free}}(e, d) R_x\left(\frac{\pi}{2}\right) U_{\mathrm{free}}(c, b) R_y\left(\frac{\pi}{4}\right), \quad [4]$$

where the strong nonselective RF pulses are assumed to lead to spin rotations of the form

$$R_\mu(\beta) = R_\mu^j(\beta) R_\mu^k(\beta), \quad [5]$$

where

$$R_\mu^j(\beta) = \exp\{-i\beta S_{j\mu}\} \quad [6]$$

and $\mu = x$, y, or z. U_{free} denotes the free precession propagator for the spin system over the time intervals $b \Rightarrow c$ and $d \Rightarrow e$, indicated in Fig. 2. Relaxation is neglected.

If the dipole–dipole coupling is neglected over the relatively short interval Δ, the pulse sequence propagator may be factorized

$$U_{3P} \simeq U_{3P}^j U_{3P}^k, \quad [7]$$

where

$$U_{3P}^j \simeq R_y^j\left(-\frac{\pi}{4}\right) U_{\mathrm{free}}^j(e, d) R_x^j\left(\frac{\pi}{2}\right) U_{\mathrm{free}}^j(c, b) R_y^j\left(\frac{\pi}{4}\right) \quad [8]$$

$$U_{3P}^k \simeq R_y^k\left(-\frac{\pi}{4}\right) U_{\mathrm{free}}^k(e, d) R_x^k\left(\frac{\pi}{2}\right) U_{\mathrm{free}}^k(c, b) R_y^k\left(\frac{\pi}{4}\right). \quad [9]$$

Here U_{3P}^j and U_{3P}^k denote individual propagators for spin j and spin k over the three-pulse sequence.

The free precession propagators are given by

$$U_{\mathrm{free}}^j(c, b) = R_z^j(\Phi^j(c, b)) \quad [10]$$

$$U_{\mathrm{free}}^k(c, b) = R_z^k(\Phi^k(c, b)). \quad [11]$$

Here $\Phi^j(c, b)$ is the integrated precession angle of spin j in the time interval $b \Rightarrow c$:

$$\Phi^j(c, b) = \Phi_{\mathrm{iso}}^j(c, b) + \Phi_{\mathrm{aniso}}^j(c, b), \quad [12]$$

where

$$\Phi_{\mathrm{iso}}^j(c, b) = \int_b^c \omega_j^{\mathrm{iso}} dt \quad [13]$$

$$\Phi_{\mathrm{aniso}}^j(c, b) = \int_b^c \omega_j^{\mathrm{aniso}}(t) dt. \quad [14]$$

In these equations, ω_j^{iso} is the isotropic chemical shift frequency of spin j, and $\omega_j^{\mathrm{aniso}}(t)$ is the instantaneous contribution of the chemical shift anisotropy to the precession frequency at time t. Similar equations apply to spin k.

In the case of exact magic-angle rotation, the integrated precession angle has the property

$$\Phi^j_{\text{aniso}}(\tau_r + t_0, t_0) = 0, \qquad [15]$$

where t_0 is an arbitrary time point and the rotor period is given by $\tau_r = |2\pi/\omega_r|$. Equation [15] corresponds to the formation of a rotational echo (51).

If the duration of the RF pulses is ignored, Eq. [15] leads to the properties

$$\Phi^j_{\text{aniso}}(c, b) + \Phi^j_{\text{aniso}}(e, d) \simeq 0 \qquad [16]$$

$$\Phi^k_{\text{aniso}}(c, b) + \Phi^k_{\text{aniso}}(e, d) \simeq 0. \qquad [17]$$

If the spectrometer reference frequency is set to the mean of the isotropic shift frequencies, then the free precession propagators are given by

$$U^j_{\text{free}}(c, b) = R^j_z\left(\frac{\pi}{2} + \theta^j\right) \qquad [18]$$

$$U^j_{\text{free}}(e, d) = R^j_z\left(\frac{\pi}{2} - \theta^j\right) \qquad [19]$$

$$U^k_{\text{free}}(c, b) = R^k_z\left(-\frac{\pi}{2} + \theta^k\right) \qquad [20]$$

$$U^k_{\text{free}}(e, d) = R^k_z\left(-\frac{\pi}{2} - \theta^k\right), \qquad [21]$$

where

$$\theta^j = \Phi^j_{\text{aniso}}(c, b) \qquad [22]$$

$$\theta^k = \Phi^k_{\text{aniso}}(c, b). \qquad [23]$$

The propagators for the three-pulse sequence may be simplified through the following reasoning:

$$U^j_{3P} \simeq R^j_y\left(-\frac{\pi}{4}\right) R^j_z\left(\frac{\pi}{2} - \theta^j\right) R^j_x\left(\frac{\pi}{2}\right) R^j_z\left(\frac{\pi}{2} + \theta^j\right) R^j_y\left(\frac{\pi}{4}\right)$$

$$= R^j_y\left(-\frac{\pi}{4}\right) R^j_z(-\theta^j) R^j_y\left(\frac{\pi}{2}\right) R^j_z(\theta^j) R^j_y\left(-\frac{\pi}{4}\right) R^j_z(\pi)$$

$$= R^j_y\left(-\frac{\pi}{4}\right) R^j_z(-\theta^j) R^j_y\left(\frac{\pi}{4}\right)$$

$$\times R^j_y\left(\frac{\pi}{4}\right) R^j_z(\theta^j) R^j_y\left(-\frac{\pi}{4}\right) \cdot R^j_z(\pi)$$

$$= \exp\left\{i\theta^j \frac{1}{\sqrt{2}}(S_{jz} - S_{jx})\right\}$$

$$\times \exp\left\{-i\theta^j \frac{1}{\sqrt{2}}(S_{jz} + S_{jx})\right\} R^j_z(\pi) \qquad [24]$$

and

$$U^k_{3P} \simeq R^k_y\left(-\frac{\pi}{4}\right) R^k_z\left(-\frac{\pi}{2} - \theta^k\right)$$

$$\times R^k_x\left(\frac{\pi}{2}\right) R^k_z\left(-\frac{\pi}{2} + \theta^k\right) R^k_y\left(\frac{\pi}{4}\right)$$

$$= R^k_y\left(-\frac{\pi}{4}\right) R^k_z(-\theta^k) R^k_y\left(\frac{\pi}{4}\right) \cdot R^k_y(-\pi)$$

$$\times R^k_y\left(\frac{\pi}{4}\right) R^k_z(\theta^k) R^k_y\left(-\frac{\pi}{4}\right) \cdot R^k_z(-\pi)$$

$$= \exp\left\{i\theta^k \frac{1}{\sqrt{2}}(S_{kz} - S_{kx})\right\} R^k_y(-\pi)$$

$$\times \exp\left\{-i\theta^k \frac{1}{\sqrt{2}}(S_{kz} + S_{kx})\right\} R^k_z(-\pi)$$

$$= \exp\left\{i\theta^k \frac{1}{\sqrt{2}}(S_{kz} - S_{kx})\right\}$$

$$\times \exp\left\{i\theta^k \frac{1}{\sqrt{2}}(S_{kz} + S_{kx})\right\} R^k_x(\pi). \qquad [25]$$

If the CSA is small compared to the spinning frequency ($|\omega^{\text{aniso}}_j \tau_r| \ll 1$, $|\omega^{\text{aniso}}_k| \ll 1$), the angles θ^j and θ^k are small. The theorem $e^{\theta A} e^{\theta B} \simeq e^{\theta(A+B)}$ allows the following approximation for the propagators:

$$U^j_{3P} \simeq R^j_x(\sqrt{2}\theta^j) R^j_z(\pi) \qquad [26]$$

$$U^k_{3P} \simeq R^k_z(\sqrt{2}\theta^k) R^k_x(\pi). \qquad [27]$$

These equations indicate that for negligible CSA, spins in the least shielded site (spins S_k) are rotated by π around the x-axis, while spins in the most shielded site (spins S_j) are rotated by π around the z-axis.

In the following discussion, we neglect the CSA of spins in the most shielded site ($\theta^j \simeq 0$). This is reasonable because spins in more shielded sites (aliphatic ^{13}C) usually have small shielding anisotropies, while spins in less shielded sites (aromatic, olefinic ^{13}C) often have large shielding anisotropies. With this approximation, the propagator for the three-pulse sequence may be written

$$U_{3P} \simeq R^j_z(\pi) R^k_z(\sqrt{2}\theta^k) R^k_x(\pi). \qquad [28]$$

This indicates that the three-pulse sequence inverts the longitudinal magnetization of spins in the less shielded site k, while compensating for the chemical shift anisotropy of that site. At the same time, the longitudinal magnetization of spins in site j is left unchanged, if the CSA of site j is neglected.
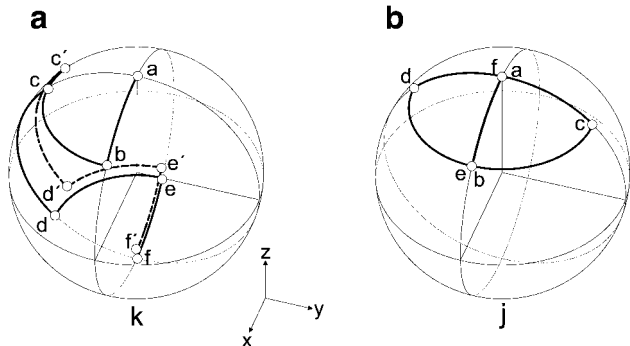
FIG. 3. Simulation of spin trajectories under the three-pulse sequence, starting with longitudinal magnetization. Plot (a) shows trajectories of the tip of the magnetization vector for the least shielded site k; plot (b) shows the trajectory for the most shielded site j. In (a) two trajectories are shown; the solid line is a simulation without CSA; the dashed line is a simulation in which the CSA is included.

The physical mechanism of the three-pulse sequence is visualized in Fig. 3. The letters a–f refer to the time points indicated in Fig. 2. It is assumed that the initial state for spins in both sites j and spins k corresponds to positive longitudinal magnetization. This state is represented by a vector along the z-axis in the rotating frame.

Figure 3a shows simulated trajectories of the tip of the magnetization vector for the spins in the least shielded site k under the three-pulse sequence. Simulations are shown for a single molecular orientation. The simulation parameters are found in Ref. (*52*). The unprimed letters a–f indicate a simulation in which the CSA is equal to zero. The primed letters (c'–f') indicate a simulation in which the CSA is taken into account.

The path $a \Rightarrow b$ shows the trajectory of the tip of the magnetization vector under the first $(\pi/4)_y$ pulse. The next rotation, $b \Rightarrow c$, indicates free evolution under isotropic chemical shifts for half a rotor period, which leads to a $-\pi/2$ rotation around the z-axis in the case of negligible CSA. The trajectory $c \Rightarrow d$ indicates the evolution under the $(\pi/2)_x$ pulse. The path $d \Rightarrow e$ shows another $(-\pi/2)_z$ rotation, generated by free evolution under the isotropic shifts. Finally, the path $e \Rightarrow f$ shows the trajectory under the last $(\pi/4)_{\bar{y}}$ pulse. This trajectory terminates exactly at the $-z$ axis if CSA effects are ignored.

The dashed path $a \Rightarrow b \Rightarrow c' \Rightarrow d' \Rightarrow e' \Rightarrow f'$ in Fig. 3a shows the motion of the magnetization vector in the case of finite CSA for site k. In this case, the rotation under $b \Rightarrow c'$ is through an angle larger than $\pi/2$, while the rotation under $d' \Rightarrow e'$ is through an angle smaller than $\pi/2$ (Eq. [16]). As may be seen, the deviations in these two rotations compensate each other to first order, leading to a final position f' which is close to the $-z$ axis. This indicates that the three-pulse sequence leads to a polarization inversion spins in sites k, which is compensated for CSA to first order.

Figure 3b shows simulated magnetization vector trajectories for spins in the most shielded site j, under the three-pulse

sequence. This simulation neglects CSA effects. From time point $a \Rightarrow b$, the $(\pi/4)_y$ pulse is applied. The following period, ($b \Rightarrow c$), denotes free evolution under chemical shifts. This leads to a rotation around the z-axis through an angle $+\pi/2$ for spins in site j. The $(\pi/2)_x$ pulse ($c \Rightarrow d$) is followed by a second period of free evolution, ($d \Rightarrow e$), which also gives a $+\pi/2$ rotation about the z-axis. The final $(\pi/4)_{\bar{y}}$ pulse brings the magnetization vector back to the positive z-axis, indicating restoration of the initial longitudinal magnetization for spins in site j.

In order for this sequence to work properly, it is essential that the signs of phase shifts and rotating-frame precession frequencies correspond. The recommendations of Refs. (*41*) and (*42*) must be followed rigorously.

These geometrical arguments apply strictly only when the three-pulse sequence is applied to longitudinal magnetization. The propagator formulation given in Eq. [28] is more general and may be applied to any state, including zero-quantum coherence.

The first three-pulse sequence in Fig. 1 is applied to transverse magnetization created by the cross-polarization sequence. Correct operation of the three-pulse sequence in this context requires that the phase of the first $\pi/4$ pulse is changed by π. The initial $(\pi/4)_{\bar{y}}$ pulse may be regarded as a contraction of a $(\pi/2)_{\bar{y}}$ pulse followed by a $(\pi/4)_y$ pulse. The $(\pi/2)_{\bar{y}}$ converts the cross-polarized transverse magnetization onto longitudinal magnetization, while the $(\pi/4)_y$ pulse forms the first element of the three-pulse sequence shown in Fig. 2 and discussed above.

Mechanical Excitation of Zero-Quantum Coherence

The zero-quantum dynamics during the interval τ may be treated using a fictitious spin-1/2 formalism (*53*). In this section, we employ the same notation for reference frames, Euler angles, and spin interaction parameters as given in Ref. (*34*).

Zero-quantum dynamics. The high field MAS Hamiltonian for an isolated spin pair in a rotating solid may be written as (*31*)

$$H = H^0 + H^{23}, \quad [29]$$

where

$$H^0 = \omega_\Sigma^{iso} S_z^{14} + \omega_A (S_z^{12} - S_z^{34}) \quad [30]$$

$$H^{23} = \omega_\Delta^{iso} S_z^{23} + \omega_B S_x^{23} \quad [31]$$

and the CSA interaction is ignored for simplicity.

The terms ω_Σ^{iso} and ω_Δ^{iso} represent the sum and difference of the instantaneous chemical shift frequencies, respectively; $\omega_\Sigma^{iso} = \omega_j^{iso} + \omega_k^{iso}$, $\omega_\Delta^{iso} = \omega_j^{iso} - \omega_k^{iso}$. The terms ω_A and ω_B are orientation dependent and represent different components of the spin–spin coupling (see below). Equations [30] and [31]

employ single-transition operators (*53*), using the basis set $|1\rangle = |+\frac{1}{2}, +\frac{1}{2}\rangle, |2\rangle = |+\frac{1}{2}, -\frac{1}{2}\rangle, |3\rangle = |-\frac{1}{2}, +\frac{1}{2}\rangle, |4\rangle = |-\frac{1}{2}, -\frac{1}{2}\rangle$.

The transformation of the dipole–dipole interaction between spins j and k from its principal axis system to the laboratory frame is specified by three Euler angle triplets, Ω_{jk}^{PM}, Ω^{MR}, and Ω^{RL}, as described in Ref. (*34*). The angles $\Omega^{MR} = \{\alpha^{MR}, \beta^{MR}, \gamma^{MR}\}$ are random variables in a powder. The angles $\Omega^{RL} = \{\alpha_0^{RL} - \omega_r t, \beta^{RL}, \gamma^{RL}\}$ specify the time-dependent relationship of the rotor frame and the laboratory frame. For exact magic-angle spinning, the second Euler angle is given by the magic-angle, $\beta^{RL} = \tan^{-1}(\sqrt{2})$.

The relevant spin dynamics during the interval τ are described by the homogeneous part of the Hamiltonian, H^{23} (Eq. [31]), which represents the interaction of the spin system with a pseudo-field in the $\{|2\rangle, |3\rangle\}$-subspace (zero-quantum space). The pseudo-field has a longitudinal component ω_Δ^{iso}, and a transverse component ω_B, which is dependent on time and orientation and is conveniently represented as a Fourier series,

$$\omega_B(t, \Omega^{MR}) = \sum_{m=-2}^{+2} \omega_B^{(m)}(\Omega^{MR}) e^{im\omega_r t}, \qquad [32]$$

where

$$\omega_B^{(m)}(\Omega_{jk}^{MR}) = -b_{jk} \sum_{m'=-2}^{2} D_{0m'}^2(\Omega_{jk}^{PM}) D_{m'm}^2(\Omega^{MR})$$

$$\times\, e^{-im\alpha_0^{RL}} d_{m0}^2(\beta^{RL}) + 2\pi J \delta_{m=0}. \qquad [33]$$

The zero-quantum part of the spin density operator may be described by a fictitious spin-1/2 vector, denoted by ρ^{23}, precessing around the pseudo-field. The longitudinal component ρ_z^{23} corresponds to longitudinal difference magnetization, while the transverse components ρ_x^{23} and ρ_y^{23} correspond to zero-quantum coherences.

At rotational resonance ($\omega_\Delta^{iso} = n\omega_r$), the frequency of the nth Fourier component of ω_B matches the frequency ω_Δ^{iso}. The magnitude and phase of the on-resonant Fourier component are denoted by the real quantities B_n and ϕ_n, with

$$\omega_B^{(n)} = B_n e^{i\phi_n}. \qquad [34]$$

Both B_n and ϕ_n are orientation dependent. In the absence of CSA, they are given by

$$B_n = |\omega_B^{(n)}| \qquad [35]$$

$$\phi_n = -n(\gamma^{MR} + \alpha_0^{RL}). \qquad [36]$$

At rotational resonance, ρ^{23} describes a complicated spiral trajectory. A simplified picture is obtained by transforming into a frame which rotates at the frequency of the on-resonant
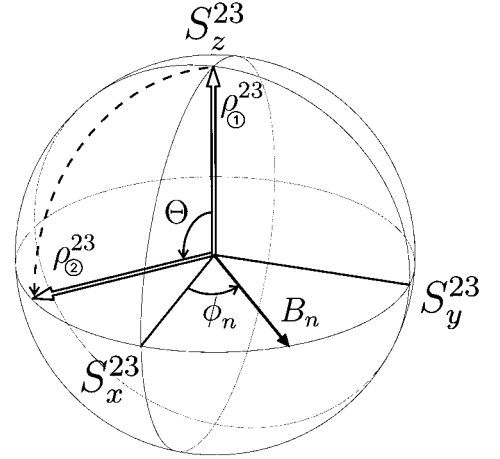

FIG. 4. Mechanical excitation of zero-quantum coherence, represented by a fictitious spin-1/2 trajectory in the rotating zero-quantum frame. The fictitious spin-1/2, ρ^{23}, initially along S_z^{23} (denoting longitudinal difference magnetization), nutates about the pseudo-field B_n through an angle Θ, toward the transverse plane (denoting zero-quantum coherence). The phase ϕ_n and magnitude B_n of the pseudo-field are determined by the direct dipole–dipole coupling and the molecular orientation.

dipole–dipole coupling component (*34*). If off-resonant terms are ignored, the vector ρ^{23} nutates around a time-independent transverse field of magnitude B_n and phase ϕ_n (Fig. 4).

The pseudo-field depicted in Fig. 4 is shown for a single molecular orientation. In a powder, a distribution of phases and magnitudes is present.

Mechanical excitation of zero-quantum coherence. The zero-quantum density matrix at time point ① (Fig. 1) is in a state of pure longitudinal difference magnetization,

$$\rho_①^{ZQ} \simeq \frac{1}{2}(S_{jz} - S_{kz}) = S_z^{23}, \qquad [37]$$

neglecting inessential factors.

The zero-quantum density operator nutates around the transverse, time-independent field B_n, in the following interval τ (Fig. 4). If relaxation is ignored, the relevant part of the density matrix at time point ② is given by

$$\rho_②^{ZQ} \simeq S_z^{23}\cos\Theta + S_x^{23}\sin\Theta\cos\phi + S_y^{23}\sin\Theta\sin\phi$$

$$= S_z^{23}\cos\Theta + \frac{1}{2}\{e^{i\phi}S_j^- S_k^+ + e^{-i\phi}S_j^+ S_k^-\}\sin\Theta, \quad [38]$$

where the amplitude and phase of the excited zero-quantum coherence are specified by

$$\Theta = B_n\tau \qquad [39]$$

$$\phi = \phi_n - \pi/2. \qquad [40]$$

Θ is the nutation angle around the effective field (Fig. 4). The maximum amount of zero-quantum coherence is produced if the nutation angle Θ is equal to $\pi/2$.

The phase angle ϕ_n and the magnitude B_n are both strongly orientation dependent. In a powder, the distribution in the value of B_n makes it impossible to achieve optimum zero-quantum excitation for all molecular orientations at the same time. However, the distribution in the value of ϕ_n is not harmful for the zero-quantum excitation. In this respect, the rotational resonance excitation of zero-quantum coherence is analogous to the excitation of double-quantum coherence by sequences such as HORROR (6) and C7 (7–10).

Excitation of Double-Quantum Coherence

The second three-pulse selective inversion sequence converts zero-quantum coherence at time point ② into double-quantum coherence at time point ③ (Fig. 1). The effect of the three-pulse sequence may be calculated using the propagator of Eq. [28]:

$$\rho_{③}^{DQ} = U_{3P}\frac{1}{2}(e^{i\phi}S_j^- S_k^+ + e^{-i\phi}S_j^+ S_k^-)U_{3P}^{-1}\sin\Theta$$

$$= -\frac{1}{2}(e^{i(\phi+\sqrt{2}\theta^k)}S_j^- S_k^- + e^{-i(\phi+\sqrt{2}\theta^k)}S_j^+ S_k^+)\sin\Theta,$$

[41]

using the transformation relationships

$$R_z(\theta)S_j^{\pm}R_z(-\theta) = e^{\mp i\theta}S_j^{\pm} \qquad [42]$$

$$R_x(\theta)S_j^{\pm}R_x(-\theta) = S_{jx} \pm i\{S_{jy}\cos\theta + S_{jz}\sin\theta\}. \qquad [43]$$

Equation [41] indicates a conversion of zero-quantum coherence into double-quantum coherence. Note that the CSA of the least-shielded spins appears as an additional phase shift of the excited double-quantum coherence by the angle $\sqrt{2}\theta^k$.

All terms in the density operator which do not correspond to double-quantum coherence have been omitted from Eq. [41]. Cycling of the radiofrequency phase suppresses signal contribution from these terms.

Conversion of Double-Quantum Coherence to Zero-Quantum Coherence

The three-pulse sequence between time points ③ and ④ converts double-quantum coherence back into zero-quantum coherence (Fig. 1).

At time point ④ we obtain the density operator

$$\rho_{④}^{ZQ} = U_{3P}\rho_{③}^{DQ}U_{3P}^{-1}$$

$$= \frac{1}{2}\{e^{i\phi}S_j^- S_k^+ + e^{i\phi}S_j^+ S_k^-\}\sin\Theta. \qquad [44]$$

The CSA-induced phase shift generated by the second three-pulse sequence is compensated by the third three-pulse sequence. The phase of the zero-quantum coherence at time point ② is preserved when it is delivered back at time point ④. This property is essential for obtaining good efficiency in a powder.

Rotational Resonance Echo of Longitudinal Difference Magnetization

The zero-quantum coherence is driven back into longitudinal difference magnetization during the evolution interval τ between time points ④ and ⑤. The zero-quantum density operator before the last $\pi/2$ pulse is given by

$$\rho_{⑤}^{ZQ} = \frac{1}{2}\{e^{i\phi}S_j^- S_k^+ + e^{i\phi}S_j^+ S_k^-\}\sin\Theta\cos\Theta - S_z^{23}\sin^2\Theta.$$

[45]

Only the last term is converted to observable transverse magnetization by the last $\pi/2$ pulse.

In the absence of relaxation, the efficiency for the entire transfer process ① ⇒ ⑤ is $\sin^2\Theta$, where Θ is given in Eq. [39]. The maximal achievable double-quantum filtering efficiency in a powder is $\simeq 73\%$, which is the same as for HORROR (6) and C7 (7). In principle, the efficiency may be further enhanced using composite pulse schemes (54).

The transfer of density operator components between the zero-quantum and double-quantum frames is sketched for a set of molecular orientations in Fig. 5. Note that the pattern of zero-quantum phases shown in diagram ② is preserved through the transfer into double-quantum coherence (diagram ③) and on reconversion into zero-quantum coherence (diagram ④). The preservation of the phase pattern is essential for the formation of the partial rotational resonance echo in diagram ⑤.

Single-Quantum Signal

Transverse magnetization is observed in the interval after the last $\pi/2$ pulse. Fourier transformation of the quadrature detected signal gives a spectrum with two peaks, with amplitudes proportional to the longitudinal magnetizations of sites j and k before the $\pi/2$ pulse. Since the spin density operator contains longitudinal *difference* magnetization at time point ⑤, the double-quantum filtered spectrum consists of one positive peak and one negative. Each peak displays a splitting, due to the recoupling of the homonuclear dipole–dipole coupling at rotational resonance.

IV. RESULTS

[$^{13}C_2$, ^{15}N]-Glycine

The spectra in Fig. 6 demonstrate the excitation of double-quantum coherence at rotational resonance for a sample of [$^{13}C_2$, ^{15}N]-glycine, in which the ^{13}C–^{13}C distance is 0.153 nm.
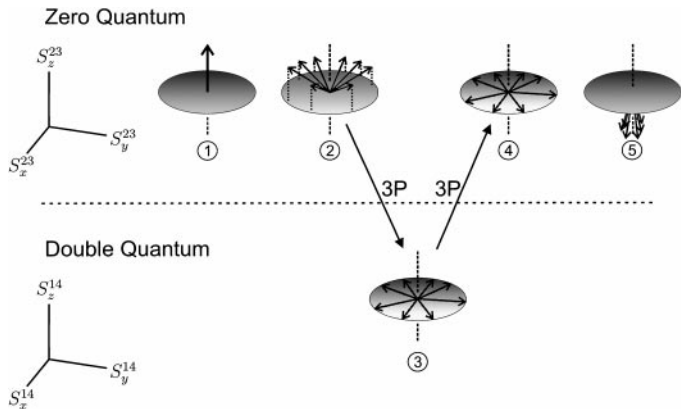
FIG. 5. Coherence transfer steps under the pulse sequence in Fig. 1. The top row represents the fictitious spin-1/2 dynamics in the zero-quantum subspace. Each vector represents the zero-quantum state for a different molecular orientation. The bottom row represents the corresponding double-quantum states. The numbers ①–⑤ denote the time points given in Fig. 1. At ①, each vector is along the S_z^{23}-axis, denoting longitudinal difference magnetization. After the excitation interval τ (time point ②), the vectors approach the transverse plane, indicating excitation of zero-quantum coherence. Zero-quantum coherence is converted into double-quantum coherence by the three-pulse sequence (② ⇒ ③), shown as a projection of zero-quantum vectors onto the double-quantum transverse plane. A second three-pulse sequence reconverts double-quantum coherence back to zero-quantum coherence, retaining the phase of each vector in the zero-quantum space. Mechanically driven evolution in the interval ④ ⇒ ⑤ leads to the formation of a rotational resonance echo of negative longitudinal difference magnetization at time point ⑤.

The two spectra were acquired under the same experimental conditions and are shown on the same vertical and horizontal scale.

The spectrum in Fig. 6a is a single-quantum spectrum obtained by ordinary cross-polarization. The spectrum displays a considerable rotational resonance splitting due to the homonuclear ^{13}C–^{13}C dipolar coupling (29). Both peaks display central features which may be attributed to imperfect heteronuclear decoupling (35). Isotopomeric impurities may also contribute.

Figure 6b is a double-quantum filtered spectrum obtained by the pulse sequence in Fig. 1, using the excitation interval $\tau =$ 363 μs. The measured peak integrals reveal a double-quantum excitation efficiency of $\simeq$56%. The rotational resonance splittings of both peaks are equal to $\omega_{split}/2\pi = 610.3$ Hz. If this splitting is converted into a distance through the semi-empirical equation of Verdegem *et al.* (14), $\gamma^2\hbar/r^3 = 3.25 \times 10^7(\omega_{split} + 14\pi)$, then the result is $r = 0.156$ nm, which is very close to the X-ray distance of $r = 0.153$ nm. In addition, note that the anomalous features in both peaks are suppressed. This behavior is not understood fully yet. In a recent analysis (35), we show that anomalous peaks in rotational resonance spectra are often associated with strongly relaxing signal components. It is likely that such strongly relaxing components give poor double-quantum excitation and hence are suppressed in the double-quantum filtered spectrum. In addition, the double-quantum filtration selects orientational components with

strong rotational resonance splittings, which are less sensitive to the relaxation effects described in Ref. (35). Any additional contributions due to isolated spin impurities are also suppressed, since isolated spins-1/2 cannot support double-quantum coherences.

[11,20–$^{13}C_2$]-all-E-Retinal

This sample is a more challenging case for double-quantum excitation, since the ^{13}C–^{13}C distance is 0.296 nm. All four spectra in Fig. 7 were acquired under the same experimental conditions.

Figure 7a shows a single-quantum spectrum of all-*E*-retinal (no isotopic labeling). The C11 and C20 peaks are indicated by arrows. The C11 peak is superimposed on a resonance from C12; the C20 peak is superimposed on a resonance from C19 (55).

The spectrum in Fig. 7b is a single-quantum spectrum of 10% [11,20–$^{13}C_2$]-all-*E*-retinal. This spectrum shows strong C11 and C20 peaks which are broadened by the rotational resonance effect.

In order to remove the natural abundance ^{13}C peaks, a weighted version of the spectrum in Fig. 7a was subtracted from the spectrum in Fig. 7b. The result is shown in Fig. 7c. The weighting factor was adjusted for optimal suppression of the natural abundance peaks. The small remaining signals are due to isotope shifts and the different linewidths in the two samples. The C11 peak in Fig. 7c reveals a typical rotational resonance lineshape, with a prominent splitting. The splitting of the C20 peak is partially obscured, as discussed in Ref. (35).

Figure 7d shows a double-quantum filtered spectrum of the 10% [11,20–$^{13}C_2$]-all-*E*-retinal sample, obtained with the
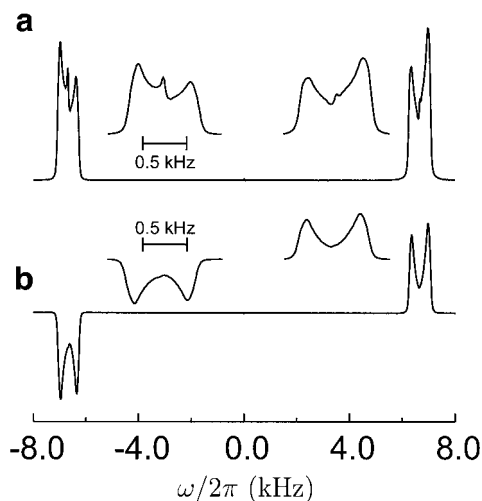

FIG. 6. Spectra of [$^{13}C_2$,^{15}N]-glycine at the $n = 1$ rotational resonance in a field of 9.4 T ($\omega_r/2\pi = 13{,}330$ Hz). (a) CP/MAS spectrum. (b) Double-quantum filtered spectrum acquired with the pulse sequence in Fig. 1 ($\tau = 363$ μs). The double-quantum filtering efficiency was 56% in this sample. Two expanded spectral regions are shown.
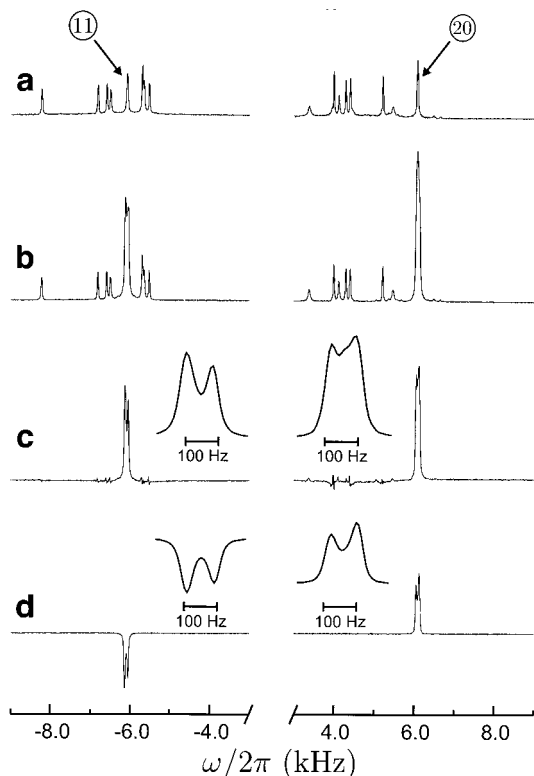
FIG. 7. Spectra of all-*E*-retinal. Each spectrum was acquired at a sample rotation frequency of 12,190 Hz, corresponding to the *n* = 1 rotational resonance between the C11 and C20 sites in the field of 9.4 T. (a) CP/MAS spectrum of natural abundance all-*E*-retinal. (b) CP/MAS spectrum of 10% [11,20–^{13}C$_2$]-all-*E*-retinal. (c) Difference spectrum of (a) and (b), with a weighting factor adjusted to remove the signals from the isolated ^{13}C spins. (d) Double-quantum filtered spectrum of 10% [11,20–^{13}C$_2$]-all-*E*-retinal obtained with the pulse sequence in Fig. 1 (τ = 2789 μs). Two expanded spectral regions are shown.

pulse-sequence in Fig. 1, using an excitation interval $\tau = 2789$ μs. The two peaks show typical rotational resonance lineshapes, with prominent splittings. The separation between the maxima of the C11 peak is 80.6 Hz: The separation between the maxima of the C20 peak is 73.2 Hz. Signal contributions from impurities are totally suppressed, and the anomalous form of the C20 peak is eliminated.

The empirical equation of Verdegem *et al.* (*14*), $\gamma^2\hbar/r^3 = 3.25 \times 10^7(\omega_{\text{split}} + 14\pi)$, may be used to estimate the ^{13}C–^{13}C distance from the peak splittings. The C11 peak splitting yields a distance estimate of 0.300 nm, while the C20 peak splitting yields 0.304 nm. Both of these estimates are rather close to the X-ray distance of 0.293 nm. These distance estimates may presumably be improved by a more rigorous analysis incorporating chemical shift anisotropy and the lineshape analysis given in Ref. (*35*).

A comparison between the peak integrals in Figs. 7c and 7d yields an estimate of 45% for the double-quantum excitation efficiency. This is remarkably high for two ^{13}C sites separated by 0.296 nm. The very high double-quantum excitation effi-

ciency is due to a very narrow zero-quantum coherence peak, i.e., negligible relaxation of zero-quantum coherence during the excitation interval. In another study (*56*), we measured the zero-quantum relaxation time constant in this sample. That experiment was performed at a spinning frequency $\omega_r/2\pi = 4.5$ kHz, under a proton decoupler level corresponding to $\omega_{\text{nut}}^I/2\pi = 90$ kHz. In that study, the zero-quantum relaxation time constant was estimated to be $T_2^{\text{ZQ}} = 32 \pm 2$ ms. The expected efficiency in the double-quantum experiment may be estimated by assuming the same value for the zero-quantum relaxation rate constant and by using the approximate decay function $\exp(-\tau/(2T_2^{\text{ZQ}}))$ for the conversion of longitudinal difference magnetization into zero-quantum coherence (*34*). The total relaxation loss over the two τ periods is expected to be only around 8%, which corresponds to a total efficiency of around 65%. The additional losses are probably due to imperfect coherence transfer by the three-pulse sequences and increased zero-quantum damping at high spinning frequency.

V. EXPERIMENTAL

Samples

[^{13}C$_2$,^{15}N]-Glycine (98% ^{13}C, 96–99% ^{15}N) was purchased from Cambridge Isotopes and used without further purification or dilution. Approximately 59 mg was packed in a Chemagnetics zirconium oxide rotor with outer diameter 4 mm.

Natural abundant all-*E*-retinal was purchased from Sigma and used without further treatment. Approximately 49 mg was packed in a 4-mm CMX-zirconium rotor.

[11,20–^{13}C$_2$]-all-*E*-Retinal was synthesized as described in Ref. (*57*). The labeled retinal was recrystallized from liquid *n*-pentane with a ninefold excess of natural abundance retinal (Fluka, Switzerland) at −80°C. Approximately 45 mg of the 10% [11,20–^{13}C$_2$]-all-*E*-retinal was packed in a Chemagnetics zirconium oxide rotor with outer diameter 4 mm.

Experiments

All experiments were performed on a Chemagnetics CMX-400 spectrometer operating at a magnetic field of 9.4 T. A Chemagnetics triple-resonance MAS probe with a 4-mm spinner module was used. The spinning frequency was stabilized to ±2 Hz. The TPPM sequences were implemented by switching the ^{1}H RF phase between the values $\pm\phi_{\text{TPPM}}$ at time intervals τ_{TPPM}. The TPPM parameters are specified for each case below.

In the experiments on the [^{13}C$_2$,^{15}N]-glycine sample (Fig. 6), the sample rotation frequency was $\omega_r/2\pi = 13\ 330$ Hz, corresponding to the $n = 1$ rotational resonance in this field. The cross-polarization interval was equal to 3.2 ms. The ^{13}C$_2$ RF field intensity was ramped (*44*). The $\pi/2$ pulse duration was 3.10 μs on the ^{1}H spins and 4.3 μs on the ^{13}C spins. During acquisition the decoupler field corresponded to the nutation frequency $\omega_{\text{nut}}^I/2\pi \simeq 109$ kHz. The TPPM parameters were $\phi_{\text{TPPM}} = 16°$ and $\tau_{\text{TPPM}} = 4.4$ μs.

In the double-quantum filtered spectrum (Fig. 6b), the decoupler field (B^1) during excitation and reconversion corresponded to a nutation frequency $\omega_{\text{nut}}^I/2\pi \simeq 151$ kHz. The TPPM parameters were $\phi_{\text{TPPM}} = 11°$ and $\tau_{\text{TPPM}} = 3.2$ μs. The excitation interval τ was equal to 363 μs. The two spectra in Fig. 6 both consisted of 32 transients, collected with an intermediate delay of 5 s.

In the experiments on all-E-retinal (Fig. 7), the sample rotation frequency was $\omega_r/2\pi = 12\,190$ Hz, corresponding to the $n = 1$ rotational resonance for the C11–C20 sites in this field. The cross-polarization interval was equal to 3 ms. The $^{13}C_2$ RF field intensity was ramped (44). The $\pi/2$ pulse duration was 3.0 μs on the ^{1}H spins and 4.5 μs on the ^{13}C spins. During acquisition the decoupler field corresponded to the nutation frequency $\omega_{\text{nut}}^I/2\pi \simeq 104$ kHz. The TPPM parameters were $\phi_{\text{TPPM}} = 15°$ and $\tau_{\text{TPPM}} = 5.4$ μs.

In the double-quantum filtered spectrum (Fig. 7d), the decoupler field (B^1) during excitation and reconversion corresponded to a nutation frequency $\omega_{\text{nut}}^I/2\pi \simeq 139$ kHz. The TPPM parameters were $\phi_{\text{TPPM}} = 7°$ and $\tau_{\text{TPPM}} = 4.3$ μs. The excitation interval τ was equal to 2789 μs. All experiments were collections of 512 transients, with a delay of 10 s between each transient, except for the spectrum in Fig. 7a, for which 4096 transients were collected.

VI. DISCUSSION

The technique presented here offers an easy and efficient method for double-quantum excitation in powdered solids. The method is feasible at high sample rotation frequencies on systems with long internuclear distances.

We envisage two major applications of this method: (i) measurement of internuclear distances; (ii) preparation of double-quantum coherences for other purposes, for example, angular estimations.

Internuclear Distance Measurements

Currently, most measurements of internuclear distances using rotational resonance have exploited the trajectories of longitudinal difference magnetization (31). This is a time-consuming procedure for several reasons: exchange experiments performed on large biomolecules often require the preparation of two different samples, one of which is selectively labeled at the spin sites of interest, and the other one is nonlabeled. The spectrum of the nonlabeled sample is used to remove the natural abundance background. Also, in order to obtain a single magnetization exchange trajectory, several individual experiments have to be carried out to trace the exchange process.

In the double-quantum filtered experiments presented here, the spectrum displays prominent splittings which should allow a direct estimation of the relevant internuclear distance through a lineshape analysis. This allows a major reduction of the experimental time compared to ordinary longitudinal differ-

ence magnetization exchange experiments. In addition, only one sample is needed in the current experiment, since the double-quantum filtration effectively suppresses the natural abundance background.

Single-quantum rotational resonance lineshapes have been analyzed to obtain internuclear distances and tensor orientations (14–16, 58, 59). However, the single-quantum rotational resonance lineshapes are considerably disturbed by relaxation phenomena (35), making the analysis of the lineshape difficult. These difficulties appear to be suppressed to a large extent in the double-quantum filtered spectra presented here. We plan to investigate this matter further.

It should also be possible to estimate spin–spin distances by measuring the amplitude of the double-quantum filtered signal as a function of one (or both) τ delays in Fig. 1. This would provide a double-quantum filtered version of the standard longitudinal magnetization exchange experiment.

Angular Investigations

The evolution of double-quantum coherences under heteronuclear local fields may be used to estimate molecular torsion angles (19–26). The experiment described here is particularly well adapted to preparation of $^{13}C_2$ double-quantum coherences in labeled peptides and proteins, since the chemical shifts of carboxyl and α-carbons are well-suited to rotational resonance studies. The HCCH and NCCN double-quantum heteronuclear local field experiments are expected to benefit from the scheme described in this paper.

In addition, the efficient long-range double-quantum excitation described here introduces further possibilities for molecular structure studies. For example, the estimation of angles between pairs of CN bonds separated by distances of 0.5 nm or more should allow study of protein secondary and tertiary structure, as well as molecular assembly and ligand binding. Efficient multiple-quantum excitation over long distances is a prerequisite for many applications of spin counting through multiple-quantum excitation (60).

Furthermore, the highly selective properties of rotational resonance should facilitate work with heavily labeled samples (18).

In this article we have concentrated on the first rotational resonance condition. The experiment could also be modified to produce double-quantum coherence at higher orders of rotational resonance. This is expected to be of importance at high magnetic fields, where the $n = 1$ rotational resonance sometimes requires an impractical spinning frequency.

The rotational resonance approach also has some strong limitations. The rotational resonance recoupling is effective only for pairs of spins with chemical shifts exactly satisfying the rotational resonance condition and with chemical shift anisotropies smaller than the isotropic shift separation. Efficient double-quantum excitation at long distances requires very well defined isotropic shifts and is intolerant of structural disorder.

In the case of large chemical shift anisotropies, the three-pulse sequence used in these experiments degrades the efficiency of the excitation of double-quantum coherence. In such systems other frequency selective inversion sequences may be contemplated (*48*).

The double-quantum filtered spectrum displays splittings due to the recoupled homonuclear dipolar interaction at rotational resonance. These splittings encode useful structural information, but also degrade the sensitivity of the experiment. We have recently developed a modification of the pulse sequence which allows the experiment to be conducted off rotational resonance (*61*). These experiments also show high double-quantum excitation efficiency and, compared to the experiments performed on rotational resonance, a further improvement in the signal-to-noise ratio.

ACKNOWLEDGMENTS

REFERENCES

1. D. P. Weitekamp, Time-domain multiple-quantum NMR, *Adv. Magn. Reson.* **11**, 111–274 (1983).

2. D. M. Gregory, M. A. Mehta, J. C. Shiels, and G. P. Drobny, Determination of local structure in solid nucleic acids using double quantum nuclear magnetic resonance spectroscopy, *J. Chem. Phys.* **107**, 28–42 (1997).

3. R. Verel, M. Baldus, M. Ernst, and B. H. Meier, A homonuclear spin-pair filter for solid-state NMR based on adiabatic-passage techniques, *Chem. Phys. Lett.* **287**, 421–428 (1998).

4. R. Tycko and G. Dabbagh, Measurement of nuclear magnetic dipole–dipole couplings in magic angle spinning NMR, *Chem. Phys. Lett.* **173**, 461–465 (1990).

5. R. Tycko and G. Dabbagh, Double-quantum filtering in magic-angle-spinning NMR spectroscopy: An approach to spectral simplification and molecular structure determination, *J. Am. Chem. Soc.* **113**, 9444–9448 (1991).

6. N. C. Nielsen, H. Bildsøe, H. J. Jakobsen, and M. H. Levitt, Double-quantum homonuclear rotary resonance: Efficient dipolar recovery in magic-angle spinning nuclear magnetic resonance, *J. Chem. Phys.* **101**, 1805–1812 (1994).

7. Y. K. Lee, N. D. Kurur, M. Helmle, O. G. Johannessen, N. C. Nielsen, and M. H. Levitt, Efficient dipolar recoupling in the NMR of rotating solids. A sevenfold symmetric radiofrequency pulse sequence, *Chem. Phys. Lett.* **242**, 304–309 (1995).

8. M. Hohwy, H. J. Jakobsen, M. Edén, M. H. Levitt, and N. C. Nielsen, Broadband dipolar recoupling in the nuclear magnetic resonance of rotating solids: A compensated C7 pulse sequence, *J. Chem. Phys.* **108**, 2686–2694 (1998).

9. C. M. Rienstra, M. E. Hatcher, L. J. Mueller, B. Sun, S. W. Fesik, and R. G. Griffin, Efficient multispin homonuclear double-quantum recoupling for magic-angle spinning NMR: ^{13}C–^{13}C correlation spectroscopy of U-^{13}C-erythromycin A, *J. Am. Chem. Soc.* **120**, 10602–10612 (1998).

10. M. Hohwy, C. M. Rienstra, C. P. Jaroniec, and R. G. Griffin, Fivefold symmetric homonuclear dipolar recoupling in rotating solids: Application to double quantum spectroscopy, *J. Chem. Phys.* **110**, 7983–7992 (1999).

11. A Brinkmann, M. Edén, and M. H. Levitt, Synchronous helical pulse sequences in magic-angle spinning NMR. Double quantum recoupling of multiple-spin systems, *J. Chem. Phys.,* in press.

12. F. Creuzet, A. McDermott, R. Gebhardt, K. van der Hoef, M. B. Spijker-Assink, J. Herzfeld, J. Lugtenburg, M. H. Levitt, and R. G. Griffin, Determination of membrane protein structure by rotational resonance NMR: Bacteriorhodopsin, *Science* **251**, 783–786 (1991).

13. O. B. Peersen, S. Yoshimura, H. Hojo, S. Aimoto, and S. O. Smith, Rotational resonance NMR measurements of internuclear distances in an α-helical peptide, *J. Am. Chem. Soc.* **114**, 4332–4335 (1992).

14. P. J. E. Verdegem, M. Helmle, J. Lugtenburg, and H. J. M. de Groot, Internuclear distance measurements up to 0.44 nm for retinals in the solid state with 1-D rotational resonance ^{13}C-MAS NMR, *J. Am. Chem. Soc.* **119**, 169–174 (1997).

15. X. Feng, P. J. E. Verdegem, Y. K. Lee, M. Helmle, S. C. Shekar, H. J. M. de Groot, J. Lugtenburg, and M. H. Levitt, Rotational resonance NMR of $^{13}C_2$-labelled retinal: Quantitative internuclear distance determination, *Sol. State NMR* **14**, 81–90 (1999).

16. P. J. E. Verdegem, P. H. M. Bovee-Geurts, W. J. de Grip, J. Lugtenburg, and H. J. M. de Groot, Retinylidene conformation in bovine rhodopsin from internuclear distance measurements using ^{13}C-labelling and 1-D rotational resonance MAS NMR, *Biochemistry* **38**, 11316–11324 (1999).

17. A. E. McDermott, F. Creuzet, R. Gebhard, K. van der Hoef, M. H. Levitt, J. Herzfeld, J. Lugtenburg, and R. G. Griffin, Determination of internuclear distances and the orientation of functional groups by solid-state NMR: Rotational resonance study of the conformation of retinal in bacteriorhodopsin, *Biochemistry* **33**, 6129–6136 (1994).

18. K. Nomura, K. Takegoshi, T. Terao, K. Uchida, and M. Kainosho, Determination of the complete structure of a uniformly labeled molecule by rotational resonance solid-state NMR in the tilted rotating frame, *J. Am. Chem. Soc.* **121**, 4064–4065 (1999).

19. K. Schmidt-Rohr, Torsion angle determination in solid ^{13}C-labeled amino acids and peptides by separated-local-field double-quantum NMR, *J. Am. Chem. Soc.* **118**, 7601–7603 (1996).

20. X. Feng, Y. K. Lee, D. Sandström, M. Edén, H. Maisel, A. Sebald, and M. H. Levitt, Direct determination of a molecular torsional angle by solid-state NMR, *Chem. Phys. Lett.* **257**, 314–320 (1996).

21. M. Hong, J. D. Gross, and R. G. Griffin, Site-resolved determination of peptide torsion angle ϕ from the relative orietnations of backbone N–H and C–H bonds by solid state NMR, *J. Phys. Chem. B* **101**, 5869–5874 (1997).

22. P. R. Costa, J. D. Gross, M. Hong, and R. G. Griffin, Solid-state NMR measurement of Ψ in peptides: A NCCN 2Q-heteronuclear local field experiment, *Chem. Phys. Lett.* **280**, 95–103 (1997).

23. X. Feng, M. Edén, A. Brinkmann, H. Luthman, L. Eriksson, A. Gräslund, O. N. Antzutkin, and M. H. Levitt, Direct determination of a peptide torsional angle ψ by double-quantum solid state NMR, *J. Am. Chem. Soc.* **119**, 12006–12007 (1997).

24. X. Feng, P. J. E. Verdegem, Y. K. Lee, D. Sandström, M. Edén, P. Bovee-Geurts, W. J. de Grip, J. Lugtenburg, H. J. M. de Groot, and M. H. Levitt, Direct determination of a molecular torsional angle in the membrane protein rhodopsin by solid state NMR, *J. Am. Chem. Soc.* **119**, 6853–6857 (1997).

25. P. V. Bower, N. Oyler, M. A. Mehta, J. R. Long, P. S. Stayton, and G. P. Drobny, Determination of torsion angles in proteins and peptides using solid state NMR, *J. Am. Chem. Soc.* **121,** 8373–8375 (1999).

26. S. Ravindranathan, X. Feng, T. Karlsson, G. Widmalm, and M. H. Levitt, Investigation of carbohydrate conformation in solution and in powders by double-quantum NMR, *J. Am. Chem. Soc.* **122,** 1102–1115 (2000).

27. A. Lesage, C. Auger, S. Caldarelli, and L. Emsley, Determination of through-bond carbon–carbon connectivities in solid-state NMR using the INADEQUATE experiment, *J. Am. Chem. Soc.* **119,** 7867–7868 (1997).

28. E. R. Andrew, A. Bradbury, R. G. Eades, and V. T. Wynn, Nuclear cross-relaxation induced by specimen rotation, *Phys. Lett.* **4,** 99–100 (1963).

29. D. P. Raleigh, M. H. Levitt, and R. G. Griffin, Rotational resonance in solid state NMR, *Chem. Phys. Lett.* **146,** 71–76 (1988).

30. M. G. Colombo, B. H. Meier, and R. R. Ernst, Rotor-driven spin diffusion in natural abundance ^{13}C spin systems, *Chem. Phys. Lett.* **146,** 189–196 (1988).

31. M. H. Levitt, D. P. Raleigh, F. Creuzet, and R. G. Griffin, Theory and simulations of homonuclear spin pair systems in rotating solids, *J. Chem. Phys.* **92,** 6347–6364 (1990).

32. N. C. Nielsen, F. Creuzet, R. G. Griffin, and M. H. Levitt, Enhanced double-quantum nuclear magnetic resonance in spinning solids at rotational resonance, *J. Chem. Phys.* **96,** 5668–5677 (1992).

33. T. Karlsson, M. Helmle, N. D. Kurur, and M. H. Levitt, Rotational resonance echoes in the nuclear magnetic resonance of spinning solids, *Chem. Phys. Lett.* **247,** 534 (1995).

34. T. Karlsson and M. H. Levitt, Longitudinal rotational resonance echoes in solid state nuclear magnetic resonance: Investigation of zero quantum spin dynamics, *J. Chem. Phys.* **109,** 5493–5507 (1998).

35. M. Helmle, Y. K. Lee, P. Verdegem, X. Feng, T. Karlsson, J. Lugtenburg, H. J. M. de Groot, and M. H. Levitt, Anomalous rotational resonance spectra in magic-angle spinning NMR, *J. Magn. Reson.* **140,** 379–403 (1999).

36. A. E. Bennett, C. M. Rienstra, M. Auger, K. V. Lakshmi, and R. G. Griffin, Heteronuclear decoupling in rotating solids, *J. Chem. Phys.* **103,** 6951–6958 (1995).

37. M. Edén and M. H. Levitt, Pulse sequence symmetries in the NMR of spinning solids: Application to heteronuclear decoupling, *J. Chem. Phys.* **111,** 1511–1519 (1999).

38. A. Khitrin and B. Fung, Design of heteronuclear decoupling sequences for solids, *J. Chem. Phys.* **112,** 2392–2398 (2000).

39. R. A. Haberkorn, R. E. Stark, H. van Willigen, and R. G. Griffin, Determination of bond distance and bond angles by solid-state nuclear magnetic resonance. ^{13}C and ^{14}N NMR study of glycine, *J. Am. Chem. Soc.* **102,** 2534–2539 (1981).

40. T. Hamanaka, T. Mitsui, T. Ashida, and M. Kakudo, The crystal structure of all-*trans* retinal, *Acta Crystallogr. B* **28,** 214–222 (1972).

41. M. H. Levitt, The signs of frequencies and phases in NMR, *J. Magn. Reson.* **126,** 164–182 (1997).

42. M. H. Levitt and O. G. Johannessen, The signs of frequencies and phases in NMR: The role of radio-frequency mixing, *J. Magn. Reson.* **142,** 190–194 (2000).

43. A. Pines, M. G. Gibby, and J. S. Waugh, Proton-enhanced nuclear induction spectroscopy. A method for high resolution NMR of dilute spins in solids, *J. Chem. Phys.* **56,** 1776–1777 (1972).

44. G. Metz, X. Wu, and S. O. Smith, Ramped-amplitude cross polarization in magic-angle-spinning NMR, *J. Magn. Reson. A* **110,** 219–227 (1994).

45. R. R. Ernst, G. Bodenhausen, and A. Wokaun, "Principles of Nuclear Magnetic Resonance in One and Two Dimensions," Clarendon Press, Oxford, 1987.

46. P. Caravatti, G. Bodenhausen, and R. R. Ernst, Selective pulse experiments in high-resolution solid state NMR, *J. Magn. Reson.* **55,** 88 (1983).

47. G. Bodenhausen, R. Freeman, and G. A. Morris, A simple pulse sequence for selective excitation in fourier transform NMR, *J. Magn. Reson.* **23,** 171–175 (1976).

48. H. Geen, M. H. Levitt, and G. Bodenhausen, Preparing initial conditions for rotational resonance in solid state NMR spectroscopy, *Chem. Phys. Lett.* **200,** 350–356 (1992).

49. M. H. Levitt, *Prog. NMR Spectrosc.* **18,** 61 (1986).

50. M. H. Levitt, Composite pulses, *in* "Encyclopedia of Nuclear Magnetic Resonance," Wiley, New York, 1996.

51. M. M. Maricq and J. S. Waugh, NMR in rotating solids, *J. Chem. Phys.* **70,** 3300–3316 (1979).

52. The simulation assumed a sample rotation frequency $\omega_r/2\pi = 5.0$ kHz. Site k was assigned the following parameters: asymmetry parameter $\eta_k = 0.5$; shift anisotropy $\omega_k^{\text{aniso}}/2\pi = 5.0$ kHz; isotropic shift $\omega_k^{\text{iso}}/2\pi = -2.5$ kHz. Site j was assigned the parameters asymmetry parameter $\eta_j = 0.5$; shift anisotropy $\omega_j^{\text{aniso}}/2\pi = 0$; isotropic shift $\omega_j^{\text{iso}}/2\pi = 2.5$. kHz. The principal axis systems of the CSA tensors were assumed to coincide with the molecular frame. The Euler angles relating the molecular frame to the rotor frame were $\Omega^{\text{MR}} = \{185°, 15°, 145°\}$.

53. S. Vega, Fictitious spin-1/2 operator formalism for multiple quantum NMR, *J. Chem. Phys.* **68,** 5518–5527 (1978).

54. T. M. Barbara, R. Tycko, and D. P. Weitekamp, Composite sequences for efficient double-quantum excitation over a range of spin coupling strengths, *J. Magn. Reson.* **62,** 54–64 (1985).

55. G. S. Harbison, P. P. J. Mulder, H. Pardoen, J. Lugtenburg, J. Herzfeld, and R. G. Griffin, High-resolution carbon-13 NMR of retinal derivatives in the solid state, *J. Am. Chem. Soc.* **107,** 4809–4816 (1985).

56. T. Karlsson, A. Brinkmann, P. J. E. Verdegem, J. Lugtenburg, and M. H. Levitt, Multiple-quantum relaxation in the magic-angle-spinning NMR of ^{13}C pairs, *Solid State NMR* **14,** 43–58 (1999).

57. M. Groesbeek and J. Lugtenburg, Synthesis of doubly and multiply isotopically labelled retinals, *Photochem. Photobiol.* **56,** 903–908 (1992).

58. S. Dusold, W. Milius, and A. Sebald, Iterative lineshape fitting of MAS NMR spectra: A tool to investigate homonuclear J couplings in isolated spin pairs, *J. Magn. Reson.* **135,** 500–513 (1998).

59. S. Dusold, H. Maisel, and A. Sebald, Magnitudes and orientations of interaction tensors determined from rotational resonance MAS NMR lineshaps of a four ^{13}C spin system, *J. Magn. Reson.* **141,** 78–90 (1999).

60. O. N. Antzutkin and R. Tycko, High-order multiple quantum excitation in ^{13}C nuclear magnetic resonance spectroscopy of organic solids, *J. Chem. Phys.* **110,** 2749–2752 (1999).

61. T. Karlsson and M. H. Levitt, Double-quantum excitation in the NMR of spinning solids by rf-assisted recoupling close to rotational resonance, submitted.